Surface circulation in the Gulf of Thailand from remotely sensed observations: seasonal and interannual timescales

Arachaporn Anutaliya[1]

[1]Institute of Marine Science, Burapha University, Chonburi, Thailand

Correspondence: Arachaporn Anutaliya (arachaporn.an@go.buu.ac.th)

Abstract. The Gulf of Thailand (GoT), a shallow semi-enclosed basin located in the western equatorial Pacific, undergoes ~~highly-variable wind influences~~ high wind variabilities on both seasonal and interannual timescales. ~~On seasonal timescale, the Asian monsoon prevails, dominating the circulation pattern. The~~ The study reveals that the surface current at different regions responds to the wind variability differently. The local Ekman pumping modifies sea level in the northern GoT, while remote wind forcing influences sea level variability at the GoT western boundary potentially through the coastal trapped Kelvin waves. The importance of wind-driven Ekman current on the ageostrophic current is also important; higher correlation between the ageostrophic and Ekman current is found toward the southern part of the GoT. The GoT circulation reverses its direction seasonally following the monsoon wind reversal; the pattern is well-captured by the most dominant complex empirical orthogonal function ~~of the Gulf of Thailand (GoT) current~~ that explains 28% of the total ~~variance with the phase relationship following the monsoon seasons. High current variability is observed over the upper GoT (uGoT),~~ circulation variance. During the monsoon transition, the circulation highlights the presence of strong meridional current along the western boundary ~~which is highly correlated with that at~~ that connects to the flow at the GoT southeastern entrance implying high exchange between the GoT and the South China Sea, and thus modification of the ~~southeastern entrance, and in the GoT interior. Satellite altimetry suggests that approximately 50% of the surface current variability is geostrophic set up by wind stress curl, particularly at basin-scale. Also, the study hints at the importance, to sea surface height near the coastline, of coastal trapped Kelvin waves forced by wind stress curl. Wind-driven current accounts for a significant fraction of the ageostrophic flow along the western boundary and the GoT interior; however, its effect is unclear over the uGoT. At~~ GoT water. On interannual timescale, the GoT circulation is directly impacted by both El Niño Southern Oscillation (ENSO) and the Indian Ocean Dipole (IOD). Interestingly, the ~~climate modes affect the circulation over each region of the GoT differently~~ two climate modes have different spatial influence on the GoT circulation. The IOD highly ~~correlates with interannual variability of~~ dominates the interannual current along the GoT western boundary and the southern boundary of the observing domain (8° N), while the ENSO correlates with that in the interior. ~~Over the uGoT, both climate modes explain similar percentage of the interannual current variability.~~

1 Introduction

The Gulf of Thailand (GoT) located at ~~6~~8°-14° N, ~~98~~99° - ~~106~~105° E (Figure ~~1~~1) is a shallow semi-enclosed basin with an average depth of 40 m that is largely influenced by winds on both seasonal and interannual timescales. On seasonal timescale,

the Asian monsoon winds prevail producing ~~a~~ the wet season over southeast Asia during the southwest monsoon (May to August) and ~~a~~ the dry season during the northeast monsoon (November to February). Although the GoT circulation also heavily dependent on inflows from the SCS, e.g., along the eastern coast of Malaysia and around the southern coast of Vietnam, these currents are also mainly driven by the monsoon winds (e.g. Wyrtki, 1961; Akhir, 2012). The extreme seasonal wind and precipitation conditions influence the circulation pattern, physical seawater properties (e.g. salinity, density, hence the thermohaline circulation; Yanagi and Takao, 1998; Yanagi et al., 2001; Buranapratheprat et al., 2002, 2008), and nutrients loadings (e.g. nitrate, phosphate, and ammonia) from rivers (Suvapepun, 1991; Sriwoon et al., 2008). Also, the location of the GoT which is to the west of the South China Sea (SCS) in the equatorial western Pacific Ocean provides a unique opportunity in observing the influence of both large-scale climate modes in the Pacific Ocean (El Niño Southern Oscillation: ENSO) and the Indian Ocean (Indian Ocean Dipole: IOD; Saji et al., 1999) on the interannual circulation.

Previous observational and numerical studies show that circulation in the Gulf of Thailand varies seasonally (e.g., Yanagi et al., 2001; Buranapratheprat et al., 2008; Saramul, 2017; Buranapratheprat et al., 2002; Aschariyaphotha et al., 2008; Saramul and Ezer, 2014). A series of 6 hydrographic cruises over October 2003 – July 2005 in the upper GoT (uGoT; north of 12.5° N) ~~suggest~~ suggests the overall cyclonic circulation during the northeast monsoon (November – February; Buranapratheprat et al., 2008) in agreement with numerical studies that accounts for tidal forcing, bottom friction, and river runoffs (Buranapratheprat et al., 2002; Saramul and Ezer, 2014). The numerical studies also suggest the dominance of contrasting anticyclonic circulation in the uGoT during the southwest monsoon (May – August). Still, both numerical simulations are forced by spatially uniform reanalysis wind products ~~,~~ which is likely not representing the actual ~~GoT wind field (Yanagi and Takao, 1998). The numerical studies also suggest the dominance of contrasting anticyclonic circulation in the uGoT~~ wind field over the region (Yanagi and Takao, 1998). A study based on numerical simulation forced by spatially varying wind (Buranapratheprat et al., 2006) emphasizes the importance of both zonal and meridional wind gradient on the circulation over the uGoT. For example, the development of an anticyclonic circulation to the north of 13° N during the southwest monsoon~~(May – August)~~, observed by Buranapratheprat et al. (2006) and Saramul and Ezer (2014), is highly dependent on the intensity of wind at the south or east of the uGoT. Results from hydrographic surveys in May 2004 and July 2005 do not show a clear dominant circulation pattern during this period (Buranapratheprat et al., 2008). High spatial-resolution coastal radar of the monthly-mean surface current during both of the southwest (June 2015) and northeast monsoon (February 2015) reveals complex circulation pattern in the uGoT, although the circulations during the two seasons are not distinctly different (Saramul, 2017). The ~~study~~ circulation based on the coastal radar suggests an overall cyclonic circulation in the northern part of the uGoT (north of 12.8°-12.9° N) and an anticyclonic circulation in the southern part (south of 12.8°-12.9° N) during both monsoon seasons.

South of 12.5° N, various observational and numerical studies were conducted (Wyrtki, 1961; Yanagi and Takao, 1998; Aschariyaphotha et al., 2008; Sojisuporn et al., 2010); however, the findings are not quite consistent due to the different studied periods and spatial resolution being considered. During the southwest monsoon, altimetry-based observation over the 1995 - 2001 period (Sojisuporn et al., 2010) shows that the circulation intensifies at the rim of the GoT with strong southward current

~~along the western boundary~~ within 1° of the GoT ~~and eastward~~ western boundary and westward current to the south of the uGoT yielding a cyclonic circulation~~within 1° of the coastline~~. At the southeastern entrance, satellite altimetry indicates an outflow into the SCS (Sojisuporn et al., 2010). Numerical simulation assimilating measurements from the NAGA expedition in 1959-1960 (Yanagi and Takao, 1998) shows similar results, except the presence of strong northwestward flow in the mid-basin which yields a cyclonic circulation to its west and an anticyclonic circulation to its east. In contrast, ~~another numerical simulation based on~~ findings from Princeton Ocean Model (Aschariyaphotha et al., 2008) ~~finds~~ indicate strong southeastward flow in the mid-basin and the dominance of an anticyclonic circulation over the GoT with an outflow at the southeastern entrance during the southwest monsoon. Note that ~~Aschariyaphotha et al. (2008) allow~~ the study by Aschariyaphotha et al. (2008) allows inflow and outflow from the lateral boundaries while ~~Yanagi and Takao (1998) do~~ that by Yanagi and Takao (1998) does not which could contribute to the discrepancy. Still, the circulation pattern found by Aschariyaphotha et al. (2008) resembles the GoT surface velocity surveyed during the NAGA expedition (Wyrtki, 1961).

During the northeast monsoon, the ~~altimetry~~ altimetric observations and numerical simulations suggest the dominance of an anticyclonic circulation at the rim of the GoT and an inflow at the southeastern entrance (Yanagi and Takao, 1998; Aschariyaphotha et al., 2008; Sojisuporn et al., 2010). Circulation in the GoT interior is quite complex and findings from the studies do not necessarily agree. The NAGA expedition, however, shows that cyclonic circulation prevails during the northeast monsoon (Wyrtki, 1961). Still, an inflow is present at the southeastern entrance in agreement with the observational and numerical studies. The inflow is found to reach the bottom at the GoT western boundary during the spring monsoon transition as cold and saline water originated in the SCS is observed there by a hydrographic survey (Yanagi et al., 2001).

Although previous studies have recognized the role of monsoon winds on seasonal variability of the GoT circulation (e.g., Yanagi and Takao, 1998; Aschariyaphotha et al., 2008), the associated dynamics are not well understood. Therefore, this study aims to examine seasonal variability of surface circulation in the GoT and the associated dynamics by investigating the influence of geostrophic current and wind-driven Ekman current using remotely-sensed observations. The mechanisms that set up the geostrophic flow will also be discussed. In addition, interannual variability of the GoT circulation will be examined to understand the effect of ENSO and the IOD on the circulation pattern.

2   Datasets

To examine circulation pattern in the GoT, the gridded Ocean Surface Currents Analyses Real-time product (OSCAR; Bonjean and Lagerloef, 2002) between 8° and 14° N, 99° and 105° E is considered (Figure 1). The product is calculated based on satellite sea surface height, wind, and water temperature from both remotely-sensed and in-situ measurements, e.g. drifters, moored, and shipboard measurements etc. The resulting current is an average in the upper 30 m of the water column. Therefore, OSCAR current represents the total current (sum of the geostrophic and ageostrophic currents) over the GoT. The gridded OSCAR prod-

uct has a resolution of 1/3° (36-37 km in the GoT) with a temporal resolution of 5 days available from 1992 to 2020. To validate

95 the OSCAR velocity over the GoT, ~~it is~~ the monthly average velocity maps in February 2015 and June 2015 are compared to tide-removed surface currents from high frequency radar system ~~(Saramul, 2017)~~ shown in Saramul (2017). Generally, OSCAR velocity exhibits similar circulation pattern to the coastal-radar velocity particularly ~~during the northeast monsoon season.~~ in February 2015. Still, much more complex circulation is observed in the coastal-radar velocity due to its much higher spatial resolution. The difference between OSCAR velocity and high-frequency coastal-radar velocity is the largest in the uGoT~~where~~

100 ~~there are only 6 OSCAR data points~~; as the region is quite small and shallow (Figure 1), the spatial resolution provided by the OSCAR products might not be sufficient to resolve the circulation there.

The gridded all-satellite merged absolute dynamic topography (ADT; η) product is used to ~~determine the importance of geostrophic current~~ calculate geostrophic current (u_g denotes zonal velocity and v_g denotes meridional velocity) in the GoT

105 and the associated mechanisms:

$$u_g = -\frac{g}{f}\frac{\partial \eta}{\partial y}, \text{ and} \tag{1}$$

$$v_g = \frac{g}{f}\frac{\partial \eta}{\partial x}, \tag{2}$$

where g represents the gravitational acceleration, f is Coriolis parameter, y is distance in the meridional direction, and x is

110 distance in the zonal direction. The product ~~is~~ interpolated daily on a 1/4° grid (27-28 km in the GoT) available over the 1993 – 2020 period (Ducet et al., 2000). As the satellite altimetry used here is in the coastal region (Figure 1), sea surface level data from ~~3~~ 7 tide gauge stations in the GoT~~, which are~~: Fort Phrachula Chomklao (FP), Ko Lak (KL), ~~and~~ Ko Mattaphon (KM), Huahin (HH), Ko Prap (KP), Laem Sing (LS), and Ko Sichang (KS) (Holgate et al., 2013; PSMSL, 2019), are used to validate the satellite-derived ADT. The comparisons show high correlation between the fluctuation of satellite ADT and the tide gauge

115 sea level over the 2014-2019 period with correlation coefficients ~~of~~ ranging from 0.69 ~~,~~ to 0.94 ~~, and 0.88 at FP, KL, and KM, respectively. The~~ (Figure 1). The ADT also shows distinct seasonal cycle consistent with water level measurements from tide gauges (Trisirisatayawong et al., 2011). The lower correlation found at FP ~~is due to its inland location, and thus locates the farthest away~~ could be due to the tide gauge's location, which locates ~20 km inland from the available gridded satellite ADT~~(~20 km)~~, or the error that the ADT might have at that location.

120

To examine the effect of wind-driven Ekman current on the GoT circulation, the gridded surface vector winds Version 2 Cross-Calibrated Multi-Platform (CCMPv2) obtained from Remote Sensing Systems are used. The CCMPv2 wind product, available from July 1987 to December 2019, has a resolution of 1/4° with a temporal resolution of 6 hours (Wentz et al., 2015). The Ekman current (u_e and v_e) at each depth (z) is calculated following Alberty et al. (2019):

125 $$u_e(z) = \frac{\sqrt{2}}{fd}e^{z/d}\left[\tau^x\cos\left(\frac{z}{d} - \frac{\pi}{4}\right) - \tau^y\sin\left(\frac{z}{d} - \frac{\pi}{4}\right)\right], \tag{3}$$

$$v_e(z) = \frac{\sqrt{2}}{fd} e^{z/d} \left[\tau^x \sin\left(\frac{z}{d} - \frac{\pi}{4}\right) + \tau^y \cos\left(\frac{z}{d} - \frac{\pi}{4}\right) \right], \tag{4}$$

where ~~f represents Coriolis parameter~~τ is wind stress, d is thickness of the surface Ekman layer defined as $\sqrt{\frac{2A}{|f|}}$ with A being a function of wind speed ~~, τ is wind stress in the zonal (x) and meridional (y) directions. In addition, wind stress curl ($\nabla \times \tau$) is also calculated from the CCMPv2 product~~($|\mathbf{U}|$; $A = 8 \times 10^{-5} |\mathbf{U}|^{2.2}$). In addition, wind stress curl ($\nabla \times \tau = \frac{\partial \tau^y}{\partial x} - \frac{\partial \tau^x}{\partial y}$) is also calculated.

The weekly sea surface temperature averaged over the Niño 3.4 box (hereafter referred to as Niño3.4) provided by the National Oceanic and Atmospheric Administration (NOAA) is used to indicates ENSO conditions (Trenberth, 1997). To assess the IOD conditions, the Dipole Mode Index (DMI) is used. The weekly DMI calculated from sea surface temperature in the tropical Indian Ocean is calculated and provided by the NOAA/ Earth System Research Laboratory (Saji et al., 1999; Black et al., 2003).

3 Methodology

To determine the dominant pattern and the associated temporal variation of the surface current in the GoT, the complex empirical orthogonal function (CEOF) is utilized. The CEOF is similar to the empirical orthogonal function (EOF) which is suitable for analysis of a dataset with both spatial and temporal variation (e.g., Weare et al., 1976; North et al., 1982). The EOF technique decomposes the data matrix that has its mean removed ($\mathbf{X}$) into orthogonal EOF modes (U) that display spatial patterns. Each mode corresponds to a time series known as the principal component (PC) that demonstrates temporal variation of that EOF mode; the PC identifies when and how intense each EOF pattern occurs. The collection of the PCs forms an orthogonal matrix (V). The matrix decomposition is done as follow:

$$\mathbf{X} = USV^T, \tag{5}$$

where the superscript T denotes the transposition of a matrix. Each EOF and PC explain different fractions of the dataset variance (variance of the i-th mode is calculated as $\frac{S_{i,i}^2}{\sum_j S_{j,j}^2}$); the first EOF mode shows the most dominant pattern and the subsequent modes account for smaller fraction of the variance by the mathematical construction. When the technique is applied to vector quantities, e.g., velocity, the CEOF is often adopted, where each vector is transformed into a complex number (e.g., Kundu and Allen, 1976; Klinck, 1985). In this study, the velocity vector with the time-mean removed ($\mathbf{u}$) is decomposed as

$$\mathbf{u} = u + iv, \tag{6}$$

where u is the zonal velocity, v is the meridional velocity, and i is $\sqrt{-1}$. Applying the same EOF technique (Eq. 5) to the complex number, the resultant PC is complex where its magnitude represents temporal fluctuation of the corresponding CEOF.

The phase calculated as arctan of the imaginary part divided by the real part represents the direction that the CEOF mode has to rotate (positive clockwise).

4 Circulation in the Gulf of Thailand

The mean and variance of OSCAR surface velocity is calculated over the 2014 - 2019 period (Figure 2). Strong mean flow is observed near the northern and western boundaries of the GoT and at the southeastern entrance. The mean current is northward along the western boundary ~~is northward~~ to the south of 12° N ~~, but southwestward or westward to the north of 12° N indicating a convergence at this latitude. The mean flow at~~ and westward at the southeastern entrance ~~is westward and southwestward transporting water from the SCS into the GoT~~ producing an outflow along the eastern boundary and an inflow along the western boundary. The mean circulation in the GoT interior consists of a few weak eddies. The mean circulation pattern from OSCAR products generally agrees with the satellite-derived geostrophic current (color contour in Figure 2a), except in the uGoT where OSCAR ~~velocity~~ products are present at only six locations. ~~OSCAR velocity has high variance along the entire~~ Also, as the uGoT is shallow and enclosed by land on the western, northern, and eastern sides (Figure 1), OSCAR products over the region could contain substantial error. Thus, discussion regarding OSCAR velocity over the uGoT will be omitted. High variance of the surface circulation is found along the western boundary of the GoT~~where~~, approximately between 9.5° and 11.5° N, with most of the ~~variability is~~ variance associated with meridional velocity ~~and at the southeastern entrance where the variability is observed for both zonal and meridional components~~ (Figure 2b). ~~Along the western boundary of the GoT, variance of~~ Variance of the ADT is also high along the western boundary indicating the influence of geostrophic flow ~~. However, the ADT variance is low~~ (Eq. 1 and 2), particularly between 9° and 10.5° N. At the southeastern entrance, high variance is also observed in both OSCAR velocity and ADT with the highest velocity variance observed at the southeastern ~~entrance highlighting the importance of ageostrophic flow that drives circulation into and out of the GoT~~ part of the observing domain and highest ADT variance observe a bit farther north, at ∼9° N.

To understand the variability of the GoT circulation, the mean surface velocity (quivers in Figure 2a) is removed from the OSCAR current to calculate Complex Empirical Orthogonal Function (CEOF~~).~~; see Methodology section). The result provides dominant circulation patterns (e.g. Figure 3a, b). Only the first 2 modes which explain 28% and 14% of the total variance are considered (Figure 3). The first ~~mode describes an anticyclonic circulation~~ CEOF mode describes a strong southward flow along the western boundary and strong southeastward flow at the southeastern entrance during the southwest monsoon and fall monsoon transition ~~in the interior of the GoT centered at~~ (Figure 3a-c). In the GoT interior, an anticyclonic circulation centered at ∼10.5° N, 101.5° E ~~with a strong southward flow along the western boundary (Figure 3a-c). Flow at the southeastern entrance of the GoT is southeastward indicating the outflow from the GoT into the SCS. In the uGoT where there are only 6 grid points in the middle of the region, the surface current is westward.~~ is present during the seasons. During the northeast monsoon and spring monsoon transition, the circulation ~~pattern reverses . The~~ reverses its direction. The circulation pattern is weaker during the monsoon transition compared to that during the monsoon seasons and it is often weak or absent at the

end of spring monsoon transition/ beginning of the southwest monsoon and at the end of fall monsoon transition/ beginning of the northeast monsoon (Figure 3b). The second CEOF mode highlights strong flow along the western boundary of the GoT with the strongest flow in the ~~uGoT~~ northern part and weaker flow toward the central and lower GoT resembling the pattern of the circulation variance (Figure 2b, 3d). Circulation in the GoT interior and along the eastern boundary is generally weak, except at the southeastern entrance. Although the phase does not exhibit a distinct pattern (Figure 3f), negative phase is found ~~between the end of~~ during the southwest monsoon and ~~early~~ into fall monsoon transition (July – October) of 2016 – 2019. The negative phase indicates southward flow along the western boundary that is strongest in the ~~uGoT area~~ northern part of the GoT and a weak ~~southward~~ southwestward flow at the southeastern entrance ~~of the GoT~~ which could associates with river runoffs (Aschariyaphotha and Wongwises, 2012). In addition, positive phase is found during the spring monsoon transition except in 2016 indicating northward flow along the western boundary and northeastward flow at the southeastern entrance which could associated with the SCS inflow (Yanagi et al., 2001; Aschariyaphotha et al., 2008).

4.1 Seasonal circulation in the Gulf of Thailand

4.1.1 Overall description

As suggested by the dominating circulation pattern calculated ~~from~~ based on CEOF, more than one quarter of the variance in the GoT current can be ~~explained by a simple~~ simply explained by an annually reversing circulation ~~pattern which is in-phase with~~ that follows the monsoon seasons (Figure 3a-c). ~~Monthly~~ Thus, monthly mean current over the 2014 – 2019 period ~~also is calculated; the monthly current~~ reveals circulation pattern generally consistent to that shown by CEOF1 (Figure 4a, c, e, g), particularly in June (representing the southwest monsoon) and December (representing the northeast monsoon). The pattern describes the circulation ~~consisting of four main regions with high variance~~ with strong current at three main regions which are the ~~uGoT, the~~ western boundary of the GoT, the interior of the GoT, and the southeastern entrance of the GoT. In the interior of the GoT, an anticyclonic circulation is present (centered at $\sim$10.5° N, 101.5° E) ~~in June and September, representing~~ during the southwest monsoon ~~and fall monsoon transition respectively~~ (Figure 4b, c). ~~Over the uGoT, the OSCAR current shows tendency of circulation pattern in the opposite direction to that in the central GoT, i. e. cyclonic during the southwest monsoonand fall monsoon transition, despite the sparse sampling locations limited to the middle part of the uGoT (Figure 2)~~Strong southward current is observed along the western boundary and strong southeastward current is observed at the southeastern entrance suggesting an outflow into the SCS at the surface. The circulation pattern generally reverses its direction during the northeast monsoon, consistent with previous surface current observation (Saramul, 2017). The monthly mean surface current hints the connection between the currents along the western boundary and that at the southeastern entrance (Figure 4a, c, e, g). ~~The current is southward~~ Thus, complex correlation analysis (Kundu, 1976) between current along the western boundary ~~, while that is southeastward at the southeastern entrance during the southwest monsoon and fall monsoon transition; circulations at both regions indicate flow out of the GoT . The opposite is observed during the northeast monsoon and spring monsoon transition, consistent with previous surface current observation (Saramul, 2017). To~~ and that over the GoT is performed using complex number constructed from velocity vector ($\mathbf{u}$, Eq. 6) to understand the dynamics associated with the strong western

boundary current particularly if it is related to the current at the southeastern entrance, ~~complex correlation analysis between current along the western boundary and that over the GoT is performed.~~ The complex correlation coefficient (R) is computed as

$$R = \frac{\mathbf{u}(t)_1 \mathbf{u}(t)_2^*}{\sqrt{(\mathbf{u}(t)_1 \mathbf{u}(t)_1^*)(\mathbf{u}(t)_2 \mathbf{u}(t)_2^*)}}, \tag{7}$$

where * denotes complex conjugate. The resultant R is a complex number where its magnitude describes how the magnitude of the two time series covary and its phase (arctan of the imaginary component divided by the real component) describes the angle between the two vector time series in order to achieve the highest correlation. On timescales longer than 30 days, currents along the southern boundary of the domain (south of 8.5° N) gives higher correlation to the western boundary current (9.0° - 11.5° N, 99.5° - 100.2° E) compared to the rest of the GoT (Figure 5); the correlation is higher than 0.25 with the highest value of 0.57 at the entrance. The correlation between the western boundary current and that along the southern boundary of the domain is significant with 95% confidence as determined by a non-parametric method (Sprent and Smeeton, 2007) where correlation coefficients are computed repeatedly (5000 times) using both of the time series that are randomly rearranged. The significant correlation strongly suggests ~~a~~ connection between the GoT western boundary current and the GoT inflow/outflow at the southeastern entrance through a passage to the south of ~8.5° N. ~~During~~

During the spring monsoon transition (represented by March), the current resembles that during the northeast monsoon; a westward flow at the southeastern entrance is observed. The cyclonic circulation in the GoT interior is still present, but weak. However, the northward flow along the western boundary is stronger and wider compared to that during the northeast monsoon; width of the northward current reaches ~100° E (Figure 4a, d). Similarly, the ~~northeast monsoon and spring monsoon transition, the~~ GoT circulation ~~generally reverses its direction~~ in September, representing the fall monsoon transition, resembles that during the southwest monsoon despite the weak anticyclonic circulation in the interior. The circulation pattern during the monsoon transitions shows the dominant circulation pattern captured by both CEOF1 and CEOF2 (Figure 3~~a)~~) reflecting the influence of both monsoon winds and the current connecting to the SCS (Figure 5).

4.1.2 Geostrophic and ageostrophic component

Satellite altimetry is used to estimate geostrophic components of the surface circulation over the GoT. Although the altimetry may include short-period contribution during the satellite over-pass, geostrophic velocity calculated from the altimetry is found to be reasonably close to the observation (Yu et al., 1995). In the Mediterranean Sea, the altimetry-derived geostrophic velocity is generally smaller than the drifter observations (Poulain et al., 2012); the error increases with the geostrophic velocity with an error of 7-17% at the velocity of 1.5 m s^{-1} (Kubryakov and Stanichny, 2013).

The satellite ADT is linearly interpolated onto the 1/3° OSCAR grid (Figure 4). Magnitude of geostrophic current is generally comparable to that of the total current, although their directions are not perfectly aligned ~~(Figure 4). The~~. Large geostrophic

velocity is observed along the western boundary of the GoT and at the southeastern entrance. The geostrophic velocity is weak in the GoT interior. The root-mean-square (rms) difference between the total and the geostrophic current (i.e. the estimated ageostrophic current) ranges from 0.04 to 0.11 m s^{-1} with the ~~median ranging from 0.03 to 0.08 m s^{-1}. The largest mismatch occurs in the uGoT and~~ largest difference observed along the western boundary of the GoT; however, the rms difference is reasonably proportional to the speed of the total current there. Complex correlation between the total and geostrophic current is calculated to determine the correlation and phase relationship between the two velocity fields (Figure 6a, b). Over the entire basin, the rms correlation coefficient is 0.70 (Figure 6a). The correlation between the total and geostrophic current is higher along the southern boundary of the observing domain, at 8° N. Along the northeastern boundary, geostrophic current only explains a small fraction of the total variance (14 – 34%). The rms correlation coefficient over the interior is 0.71 ~~, while those averaged over the uGoT and the western boundary are lower with values of 0.63 and~~ and that over the western boundary region is 0.67~~, respectively~~. The strong correlation indicates the dominance of geostrophic circulation over the GoT. Phase relationship shows the direction that the geostrophic current has to rotate to align with the direction of the total current where positive denotes counterclockwise rotation. ~~In the central and lower GoT (south of 12° N), a~~ A negative phase relationship is found roughly ~~to the north of~~ between 10.5° and 12° N while a positive relationship is found to the south of 10.5° N (Figure 6b). With the ~~dominating~~ presence of anticyclonic circulation centered at 10.5°-11° N during the southwest monsoon and fall monsoon transition, the phase relationship requires southeastward ageostrophic flow. In contrast, the phase relationship implies northwestward ageostrophic current during the northeast monsoon and spring monsoon transition when cyclonic circulation dominates the GoT interior. As the prevailing monsoon wind is southwesterly during the southwest monsoon and northeasterly during the northeast monsoon, the resulting wind-driven Ekman current aligns with the direction of the ageostrophic flow in the respective seasons. ~~This reflects the importance of the wind-driven Ekman flow on the GoT circulation, although the~~ Therefore, the Ekman ~~velocity~~ current is calculated from the CCMPv2 wind (Eq. 1 and 2) and compared with the ageostrophic current.

Wind-driven Ekman current averaged in the upper 30 m of the water column (or to the seafloor where the water column is shallower than 30 m) ~~computed from the CCMPv2 wind is generally smaller than the ageostrophic current. The rms of monthly wind-driven Ekman current ranges from 0.01 to 0.05 m s^{-1} with a similar range in median~~ has a distinct seasonal cycle being strongest during the northeast monsoon and the weakest during the spring monsoon transitions (Figure 4b, d, f, h). ~~In the uGoT,~~ During the northeast monsoon, speed of the Ekman current exceeds 0.06 m s^{-1} almost everywhere except between 10° - 12° N along the eastern coast. The weak Ekman current is likely due to the presence of the Cardamom Mountains between 10° - 13° N at the coast of Thailand and Cambodia that blocks the northeasterlies (Li et al., 2014). The strongest current is at the southeastern entrance with the speed of 0.1 m s^{-1} transporting water into the GoT (Figure 4h). The Ekman current at the southeastern entrance still transports water into the GoT during the spring monsoon transition, although the speed decreases due to the ~~correlation coefficient between~~ weakening of the monsoon wind (Figure 4b). During the ~~geostrophic and total currents is also high and significant with 95% confidence (Figure 6a). The phase relationship is mainly positive (Figure 6b)indicating westward (northward) ageostrophic current during the southwest (northeast) monsoon . During the fall monsoon transition, the positive phase relationship implies southward ageostrophic current. Compared to results~~

~~from a numerical study which indicates circulation in the direction of the expected wind-driven current over the uGoT (i. e.~~
290 ~~anticyclonic during the~~ southwest monsoon and ~~cyclonic during the northeast monsoon) (Buranapratheprat et al., 2002), the~~ ~~circulation based on the remotely sensed observations is not quite consistent. The inconsistency could reflect forcings neglected~~ ~~by the numerical simulation that is included in the remotely sensed observation, e. g. the spatially-variant wind pattern and~~ ~~form drag (MacCready et al., 2003). Also, the difference in circulation patterns could be attributed to the insufficient spatial~~ ~~resolution of the observations over such a small area with shallow bathymetry. During the spring monsoon transition, the~~
295 ~~ageostrophic current is northward in the same direction to that of the wind-driven Ekman current, although the calculated~~ ~~wind-driven current is smaller than the ageostrophic current (Figure~~ fall monsoon transition, the Ekman current is quite uniform over the entire GoT; the flow is southeastward producing an outflow into the SCS (Figure 4~~b)~~d, f). Magnitude of the Ekman current is similar to the ageostrophic current in the GoT interior and the southeastern entrance, but smaller along the boundaries.

300 Complex correlation between the ageostrophic component and wind-driven Ekman current is calculated to examine the contribution of wind-driven current on the ageostrophic circulation (Figure 6c). Higher correlation is found over the southern part of the domain with the highest correlation coefficient of 0.54 reflecting that up to 29% of the ageostrophic circulation is wind-driven. Over the western boundary region, the correlation coefficient between the wind-driven current and the ageostrophic current is 0.40. Similar value of correlation coefficient is observed over the interior of the GoT (~~r~~ R = 0.41). ~~The uGoT is one~~
305 ~~of the regions where the wind-driven current only explains a small percentage of total variance in ageostrophic flow; r = 0.20,~~ ~~significant with 95% confidence.~~ Phase relationship indicates the direction that the Ekman current has to rotate to align with the direction of the ageostrophic current; it is small overall with most values between $-\frac{\pi}{4}$ and $\frac{\pi}{4}$ (Figure 6d). When ageostrophic current is entirely driven by wind stress, the phase relationship is zero. Thus, the small phase relationship hints the importance of forcings other than wind stress on ageostrophic current, e.g. counterflow produced by the bottom friction (the bottom Ekman
310 layer), etc. Negative phase is only found in a narrow band along the northwestern boundary ~~reflecting~~ indicating that wind-driven current is to the left of ageostrophic flow. The negative phase is clearly evident in June~~and December when monsoon~~ ~~winds are strong, while it is not clear during the monsoon transitions (March and September)~~, September, and December, while a positive phased is suggested during the spring monsoon transition (March) (Figure 4b, d, f, h).

315 Although the spatial resolution of the OSCAR products is too coarse to capture the complex circulation over such small and shallow basin as the uGoT, previous studies have described the general circulation (Yanagi et al., 2001; Buranapratheprat et al., 2006, 2008; and thus speculation on the interaction between the uGoT and the rest of the GoT can be provided. During the southwest monsoon, southward flow is present along the western boundary to the south of ∼12.5° N (Figure 4c) and the uGoT circulation is anticyclonic; thus, the flow along the western boundary is likely not continuous into the uGoT and a divergence likely
320 occurs at the coast. Instead, the northward flow along the western boundary of the uGoT is likely supplied by the western flank of the anticyclonic circulation in the GoT interior transporting high salinity (Buranapratheprat et al., 2002) and low nutrient (Buranapratheprat et al., 2009) water into the uGoT. The current at the southeast of the uGoT that is eastward/ northeastward opposing the southward flow along the uGoT eastern boundary yielding a convergence. During the northeast monsoon,

cyclonic circulation is present over the uGoT. The southward flow along the uGoT western boundary potentially continues southward joining the western flank of the cyclonic circulation in the GoT interior (Figure 4~~a-d).~~ g). Along the uGoT eastern boundary, the northward current is supplied by water from lower latitudes with relatively high salinity and low-nutrient (Buranapratheprat et al., 2002, 2009). The water mass is likely derived from the westward/ northwestward flow between 11° and 12° N that bifurcates to have one flank travels northward along the uGoT eastern boundary while the other continues westward serving as the northern flank of the GoT interior cyclonic eddy.

4.1.3 The role of wind stress curl on the sea surface height

The impact of the wind stress curl on sea surface height is examined through a linear regression using daily measurements ~~. The~~ at the original spatial resolution of 1/4°. Both of the basin-averaged wind stress curl and ADT have distinct seasonal cycle~~consistent with water level measurements from tide gauges (Trisirisatayawong et al., 2011)~~; high (low) ADT is observed during the northeast (southwest) monsoon over the entire basin, while the wind stress curl exhibits the opposite pattern (Figure 7a). In addition, the intraseasonal signals of the basin-averaged ADT covary quite well with the basin-averaged wind stress curl. The anticorrelation yields a significant negative correlation of -0.84 ~~reflecting~~ indicating the dominance of wind stress curl on the ADT through local Ekman pumping; positive (negative) wind stress curl induces upward (downward) flow in the water column and depresses (raises) the ADT. ~~The high anticorrelation reflects the~~ In addition, the correlation suggests no time lag between the wind curl and the ADT reflecting the instantaneous adjustment of the ADT as being forced by the local wind stress curl. As Zhou et al. (2012) suggest a delayed response of the ADT to wind stress curl over the SCS (decaying timescale of ~~-~~~40 days), the result demonstrates the different wind-associated dynamic that underlies the GoT compared to the rest of the SCS.

As most energy of the GoT circulation locates along the western boundary of the GoT (Figure 2, 3, 4), the influence of wind stress curl on current variability at 9.6° N, 99.9° E representing high ADT variance ~~in the~~ to the south of the uGoT (purple cross in Figure 2b) and 12.9° N, 100.1° E representing high variance along the western central GoT (green cross in Figure 2b) are further investigated. ~~Correlation coefficient is calculated~~ Since an effect of winds on the ocean circulation is not necessarily local nor applied over a large scale (e.g. Meyers, 1996; Giddings and MacCready, 2017), relationship between ADT at ~~each selected location~~ the selected locations and wind stress curl over the entire GoT is examined to identify the location of wind stress curl that influences the ADT. ADT with high variance ~~over~~ south of the uGoT correlates well with the nearby wind stress curl ~~over the uGoT~~ with a correlation coefficient of -0.80 suggesting a local response of ADT and thus the geostrophic current on the wind stress curl, although much of the correlation ~~attributes~~ is attributed to the dominant seasonal cycle observed in both variables (Figure 2b, 7c). However, high-variance ADT at the western boundary is correlated with wind stress curl ~~-~~~280 km to its north (Figure 2b, 7b). Wind stress curl to the south of the uGoT (12.1° N, 100.1° E) explains 80% of the ADT variance at the central part of the GoT western boundary (9.6° N, 99.9° E) as it also captures intraseasonal fluctuation of the ADT. The mechanism associated with high correlation between ADT at the western boundary and remote wind stress curl is still unclear and beyond the scope of this study. Still, the result suggests the importance of coastal trapped Kelvin waves which travel

equatorward along the western boundary of the basin .(Wang, 2002). Coastal trapped Kelvin waves are also commonly found in regions with shallow and complex bathymetry, e.g., the Indonesian Archipelago (Sprintall et al., 2000; Delman et al., 2018) and the SCS and the East China Sea (Wang et al., 2003; Yin et al., 2014; Liu et al., 2011). At the GoT interior, wind stress curl does not exhibit seasonal cycle, and thus, the local wind stress curl does not locally influence the ADT there.

4.1.4 Interaction with the South China Sea

Since the GoT connects to the SCS, variability of the SCS circulation would provide a better understanding on the GoT circulation as well as origin of water masses transported into the basin. In the southern part of the SCS, the circulation is highly influenced by the monsoon winds (e.g. Hu et al., 2000; Gan et al., 2006). During the northeast monsoon when the inflow from the SCS to the GoT is observed (Figure 4g), a strong southwestward flow is present off the eastern coast of Vietnam; the current partly turns northwestward transporting water into the GoT (Hu et al., 2000; Gan et al., 2006; Liu et al., 2008). Thus, the GoT largely is replenished by water from the northern SCS which is highly influenced by the Kuroshio intrusion (Chao et al., 1996; Jilan, 2004; Wang et al., 2006; Centurioni et al., 2009). As the Kuroshio intrusion path can be quite variable, the northern SCS circulation varies depending to the intrusion path (Hu et al., 2000; Caruso et al., 2006; Nan et al., 2015) which potentially contributes to variability of the GoT circulation, particularly at the entrance. During the southwest monsoon, a northwestward flow is present to the south of the GoT and the current off Vietnam coast reverses to flow northwestward (Hu et al., 2000; Gan et al., 2006; Liu et al., 2008). The observed GoT outflows during the southwest monsoon and fall monsoon transition likely join the northwestward flow transporting freshwater from river runoffs (Aschariyaphotha and Wongwises, 2012) into the SCS.

4.2 Interannual variability of the circulation in the Gulf of Thailand

The influences of ENSO and IOD are examined to understand interannual variability of the GoT circulation. Low-frequency OSCAR velocity is calculated by removing the seasonal cycle, taken as a linear combination of annual and semiannual harmonics that best fit the 6-year observations, and signals with periods shorter than 90 days. A 90-day lowpass filter is also applied to sea surface temperature averaged over the Niño 3.4 box (hereafter referred to as Niño3.4) which indicates ENSO conditions and Dipole Mode Index (DMI) which indicates IOD conditionsand DMI (see Datasets section). Complex correlation between the low-frequency indices, which have a phase of zero ($\pm\pi$) for a positive (negative) value, and the low-frequency currents is calculated over the entire GoT (Figure 8a, b). The correlation shows fascinating patterns revealing that the ENSO conditions highly influence the circulation over the central and the eastern parts of the GoT, while IOD conditions influence the current along the western boundary of the GoT and the southern boundary of the observing domain.

The low-frequency zonal current averaged over the uGoT (12.5° - 13.5° N, 100.0° - 101.0° E) correlates with the low-frequency Niño3.4 with a correlation coefficient of -0.29 (significant at the 95% confidence level); the current is anomalously westward (eastward) during an El Niño (La Niña) event (Figure 9a). During the 2015/2016 El Niño, the area-averaged current anomaly is generally westward; still, the current anomaly fluctuates quite a bit which contributes to the low correlation. The current is

anomalously eastward during the 2017/2018 La Niña. To understand the dynamics associated with the low-frequency variability of the GoT circulation, correlations between low-frequency Niño3.4 and selected forcings, which are ADT, zonal wind stress, and wind stress curl, are calculated (Figure 8c, e, g). Similarly, those between DMI and the selected forcing are also computed (Figure 8d, f, h). Note that the meridional wind stress is also considered; however, its correlation with either of the indices

395 does not exhibit a distinct variation pattern over the GoT. The mechanism associated with the low-frequency zonal current variability over the uGoT during ENSO conditions is, however, unclear as the local low-frequency ADT, wind stress, and wind stress curl do not suggest a negative relationship between the current and Niño3.4. The correlation map implies a positive ADT gradient anomaly eastward during an El Niño condition (Figure 8c), which is influenced by the local wind stress curl (Figure 8g), resulting in a northward current anomaly. The low-frequency zonal wind over the uGoT tends to be eastward producing

400 a southeastward current anomaly (Figure 8e), while the meridional wind stress tends to be positive yielding a northeastward anomaly (not shown). During La Niña conditions, the uGoT current anomaly and anomalies of the selected forcings tend to reverse their direction. A higher and positive correlation of 0.39 is found between the area-averaged zonal current and DMI suggesting the tendency of eastward (westward) zonal current anomaly during a positive (negative) IOD phase (Figure 9a). The expected anomalous current pattern is observed during both the 2016 negative IOD and 2019 positive IOD events. The positive

405 relationship is largely geostrophic as the low-frequency ADT gradient is positive southward (northward) over the uGoT during an El Niño (a La Niña) producing eastward (westward) geostrophic current (Figure 8d). The ADT pattern is likely influenced by local wind stress curl as a positive curl lowers the ADT and a negative curl elevates it (Figure 8h). Note that the interannual meridional velocity averaged over the uGoT is also considered; however, it does not correlate well with the climate modes (not shown).

410 Along the western boundary of the GoT, high correlation between the low-frequency current and low-frequency DMI is found with a phase relationship of $\frac{\pi}{2}$ indicating northward (southward) current anomaly during a positive (negative) IOD condition (Figure 8b). The low-frequency alongshore meridional current averaged in 9.0° - 11.5° N, 99.5° - 100.2° E region is used to represent the current along the western boundary; low-frequency DMI explains 45% of the variance of the alongshore meridional flow (Figure 9b). During the 2016 negative IOD event, the southward western boundary current (Figure 4)

415 intensifies during the southwest monsoon and fall monsoon transition. In contrast, the seasonal southward current significantly weakens during the southwest monsoon and fall monsoon transition of 2019 when a positive IOD occurs. The In addition, DMI correlates with the OSCAR current along the southern boundary of the domain. With the phase relationship of approximately ±π, the current is westward (eastward) along ∼8° N during a positive (negative) IOD event. The result suggests that IOD events does not only affect the current along the western boundary but they impact the continuous current from the southeastern

420 entrance to the western boundary of the GoT (Figure 3-5). The results are opposite to the finding by Higuchi et al. (2020) that suggests an anomalous outflow during the southwest monsoon season of a positive IOD event. To understand the dynamics associated with the low-frequency variability of the current GoT circulation, correlations between low-frequency DMI and selected forcings, which are ADT, zonal wind stress, and wind stress curl, are calculated (Figure 8c, e, g). Similarly, those between Niño3.4 and the selected forcing are also computed (Figure 8d, f, h). Note that the meridional wind stress is also

425 considered; however, its correlation with either of the indices does not exhibit a distinct variation pattern over the GoT. The

low-frequency variability of the current along the western boundary during IOD events is likely associated with local zonal wind stress (Figure 8f). Low-frequency component of the zonal wind stress shows strong correlation with the DMI along the GoT western boundary with correlation coefficients of up to -0.75 and along the southern boundary of the domain with correlation coefficients of up to -0.58; the correlation pattern is similar to that between the OSCAR current and DMI (Figure 8b). The negative correlation suggests the westward (eastward) wind stress anomaly during a positive (negative) IOD event yielding a northwestward (southeastward) surface Ekman current anomaly along the western boundary, consistent with the low-frequency OSCAR current. Although the low-frequency wind stress curl and ADT also suggest northward flow anomaly along the western boundary, the influence is roughly the same along the entire western boundary as well as the eastern boundary (Figure 8d, f). Therefore, the low-frequency variability of the current along the GoT western boundary is likely not associated with the ADT and wind stress curl variability during IOD conditions. Correlation between low-frequency Niño3.4 and low-frequency alongshore meridional current is small (r R = 0.14) but significant with 95% confidence suggesting a tendency of northward (southward) current anomaly during an El Niño (La Niña) event; however, the current anomaly is not clearly apparent during the 2015/2016 El Niño and the 2017/2018 La Niña (Figure 9b).

In the GoT interior, a region of high correlation between Niño3.4 and OSCAR current is found at ~10.0° - 11.0° N, 100.5° - 103.0° E (the northern dashed box in Figure 8a), with the out-of-phase relationship that indicates westward current anomaly during an El Niño event and eastward current anomaly during a La Niña event. Considering low-frequency zonal current averaged over the region, Niño3.4 explains 34% of the low-frequency variance of the zonal flow (Figure 9c). With a 75-day lag of the area-averaged current, the correlation improves to -0.71; half of the variance in low-frequency zonal current at this region is associated with ENSO condition. Along the southern boundary of the domain (~8° - 9° N, 101.5° - 104.0° E), the correlation is also high and significant with 95% confidence. However, the relationship is in-phase indicating an eastward (westward) current anomaly during an El Niño (a La Niña) event. This results in a weak GoT inflow at the southeastern entrance during an El Niño event consistent with weak circulation found in the SCS (Chao et al., 1996; Wang et al., 2006). The low-frequency Niño3.4 explains 14% of variance in the area-averaged low-frequency zonal current with no lag (Figure 9c). This opposing pattern suggests a cyclonic current anomaly in the GoT interior during an El Niño and an anticyclonic anomaly during a La Niña with its location further farther south than the seasonal cyclonic and anticyclonic circulation (Figure 3, 4a, c). The low-frequency cyclonic (anticyclonic) circulation during an El Niño event (a La Niña) colocates with anomalously low (high) ADT suggesting the dominance of geostrophic flow response in the GoT interior to ENSO variability (Figure 8c). The mechanism setting up the low-frequency ADT variability is unclear; it cannot be explained by local wind stress and wind stress curl (Figure 8e, g) but might relate to the winter warm pool located at the eastern boundary of the GoT (Li et al., 2014). Still, the influence of low-frequency wind stress curl on the ADT through coastal trapped Kelvin waves cannot be eliminated. The correlation map suggests negative (positive) wind stress curl at the GoT eastern boundary between 8.5° and 11.5° N during an El Niño (La Niña) creating positive (negative) ADT anomaly that could propagate northward in the form of coastal trapped Kelvin waves. The cyclonic circulation is clearly observed following During the 2015/ 2016 El Niño, particularly during the 2015/2016 northeast monsoon, the cyclonic circulation centered at 9.7° N, 101.7° E is clearly apparent during the northeast monsoon and

the 2016 into the spring monsoon transition (Figure 9c);., while the seasonal cyclonic eddy locates further south centered at 9.5circulation centered at 10.5° N, 102.0101.5° E ,is missing (Figure 3-4). Therefore, the seasonal cyclonic circulation locates farther south during the El Niño event. Shortly after the peak of the 2017/2018 La Niña, an anticyclonic anomaly centered at the same location (centered at 9.7° N, 101.7° E) develops (Figure 9c). The anticyclonic eddy anomaly in the GoT interior becomes more pronounced during the 2018 spring monsoon transition when the La Niña decays. The low-frequency DMI is significantly correlated with low-frequency zonal current in the interior. However, it explains less than 5% of the low-frequency zonal current variance and the general circulation pattern away from the western boundary and the uGoT do not show a significant deviation from the seasonal current during the negative IOD event in 2016 and positive IOD event in 2019 (Figure 8b, 9c), although Higuchi et al. (2020) suggest an anomalous outflow at the entrance during the southwest monsoon of positive IOD events.

The ADT, zonal wind stress, and wind stress curl are also examined over the uGoT region to understand how these forcings, which potentially influence the uGoT interannual circulation, vary during the ENSO and IOD events (Figure 8). Positive correlation is found between the ADT over the uGoT and Niño3.4 indicating a tendency of an anomalously high (low) sea level, particularly along the eastern boundary during an El Niño (La Niña) event (Figure 8c). The pattern is consistent with that produced by the wind stress curl (Figure 8g). Therefore, the geostrophic current is likely anomalously northward (southward) along the western boundary of the uGoT. In addition, a positive correlation between the zonal wind stress and Niño3.4 is present reflecting anomalously southward (northward) wind-driven Ekman current during an El Niño (La Niña). Correlations between the selected forcings and DMI are generally lower than when compared to the Niño3.4 (Figure 8c-h). A southward geostrophic flow along the eastern boundary of the uGoT and an eastward flow to the south of the uGoT are expected due to the stronger positive correlations between DMI and ADT along the uGoT eastern boundary and the southern part of the uGoT compared to that over the northwestern part (Figure 8d). A positive correlation between DMI and wind stress curl is also found over the uGoT potentially contributing to a lower increase in the sea level compared to that in the rest of the GoT where negative correlation is present (Figure 8f). IOD events are overall not significantly correlate to the zonal wind stress over the uGoT (Figure 8f).

5   Conclusions

This study exploits the synergy of available remotely-sensed observations to understand variability of the GoT circulation under the influence of highly variable winds at the seasonal and interannual timescales. At the interannual timescale, surface circulation over the GoT responds to that reveals different responses to the different climate modesdifferently. The .. The interannual current along the western boundary is more sensitive to IOD conditions, while that in the GoT interior is more sensitive to ENSO conditions (Figure 8, 9). At the seasonal timescale, the observation reveals spontaneous adjustment of the basin-averaged ADT following basin-averaged wind stress curl signal that is different from the rest of the SCS (Zhou et al.,

2012). Still, the associated mechanisms are different over different parts of the GoT (Figure 7). For example, the ADT at the southern part of the uGoT highly correlates with the local wind stress curl reflecting the influence of local Ekman pumping, while the ADT along the western boundary is highly related with the wind stress curl to its north ~~reflecting~~ suggesting the influence of ~~remote forcing.~~ coastal trapped Kelvin waves on modifying the sea level along the western boundary. Similar to circulation in the SCS (Gan et al., 2006), current over the GoT is mostly geostrophic. The ADT variability sets up the surface geostrophic flow which accounts for approximately half of the surface current variability (Figure 4, 6). The ageostrophic current is significantly explained by the Ekman current, although the portion being explained varies from one region to another. The Ekman current accounts for a larger percentage of the ageostrophic flow along the western boundary and the GoT interior, particularly to the south of ~~-~~~$\sim$10° N, compared to region to the north of this latitude.

The OSCAR surface current product also ~~reveals~~ demonstrates the seasonal reversing circulation pattern at the surface following the monsoon wind reversal that accounts for 28% of the total current variance over the 2014 - 2019 period (Figure 3a-c). The seasonal pattern confirms the anticyclonic circulation in the GoT interior with an outflow at the southeastern entrance during the southwest monsoon (Figure 4) consistent with findings from ~~Wyrtki (1961); Sojisuporn et al. (2010); Aschariyaphotha et al. (2008)~~ Wyrtki (1961); Sojisuporn et al. (2010); and Aschariyaphotha et al. (2008). A cyclonic circulation along the western boundary of the GoT as suggested by a numerical simulation (Yanagi and Takao, 1998) is present but narrow, confined to the west of ~~-~~~$\sim$100.5° E. Also, the western flank of the cyclonic circulation is stronger than the eastern flank consistent with a previous altimetric observation (Sojisuporn et al., 2010). During the northeast monsoon, OSCAR product shows strong northward flow along the western boundary and an inflow at the southern entrance consistent with observational (Sojisuporn et al., 2010) and numerical studies (Yanagi and Takao, 1998; Aschariyaphotha et al., 2008) that suggest anticyclonic circulation over the GoT. ~~However, the~~ The 6-year averaged surface velocity displays the dominance of cyclonic circulation in the GoT interior (Figure 4), in agreement with that observed during the NAGA expedition (Wyrtki, 1961). ~~As the uGoT is shallow and enclosed by land on the western, northern, and eastern sides, the derived surface circulation could contain substantial error. Also, OSCAR observation is quite sparse in the uGoT and along the coastline; it does not fully capture the complex circulation at these regions (Figure 1~~

In addition, the finding reveals the importance of the GoT circulation during the monsoon transitions that shows the presence of strong seasonal meridional flow along the western boundary and the southeastern entracen. The strong northward flow along the western boundary that superimposes on the circulation pattern during the northeast monsoon is found during the spring monsoon transition (Figure 3-4). During the fall monsoon transition, southward flow is present along the western boundary and strong southeastward current is observed at the southeastern entrance. As the western boundary current is connected to that at the southeastern entrance (Figure 5), ~~4). Therefore, finer resolution observations are critical to understand the circulation pattern in the uGoT and along the coast.~~ the results highlight the connection between circulation in the GoT and the SCS that distinctly occurs during the monsoon transitions. Moreover, variability of the circulation during the transition seasons could

largely impact the properties of water in the GoT.

530   Although this study offers insightful details of the GoT circulation, particularly to the south of 12.5° N, there are still forcings that are not considered, for example, tidal currents and planetary waves. Previous studies have indicated the importance of tidal pattern over the GoT that is different from one region to another (Yanagi and Takao, 1998) and is heavily dependent on tidal pattern in the SCS (Cui et al., 2019). The effect of coastal trapped Kelvin waves on the coastal circulation which is also observed in the nearby regions ~~, e.g. the SCS and the East China Sea (Wang et al., 2003; Yin et al., 2014; Liu et al., 2011)~~

535   , (Sprintall et al., 2000; Wang et al., 2003; Yin et al., 2014; Liu et al., 2011; Delman et al., 2018), cannot be concluded despite the observed influence of remote wind stress curl on the western boundary current. ~~Moreover, the interaction between the SCS and GoT is still unknown.~~ Thus, examination of these factors could further improve the understanding of dynamics associated with the GoT circulation.

Data availability. The OSCAR third degree Version 1 data are provided by Physical Oceanography Distributed Active Archive Center.

540   CCMP Version-2.0 vector wind analyses available at www.remss.com are produced by Remote Sensing Systems. This study has been conducted using E.U. Copernicus Marine Service Information (http://marine.copernicus.eu/services-portfolio/access-to-products/?option=com_csw&view=details&product_id=SEALEVEL_GLO_PHY_L4_REP_OBSERVATIONS_008_047). Niño 3.4 and DMI are available at https://www.cpc.ncep.noaa.gov and https://stateoftheocean.osmc.noaa.gov/sur/ind/dmi.php, respectively.

Author contributions. The author confirms contribution to the paper as follows: data collection: A. Anutaliya; data analysis: A. Anutaliya;

545   discussion of results: A. Anutaliya.

Competing interests. The author declares no relevant competing interests.

Acknowledgements. This work has been supported by the 2021 Research Grant of Burapha University under grant 001/2564 to Arachaporn Anutaliya.

References

550   Akhir, M.: Surface Circulation and Temperature Distribution of Southern South China Sea from Global Ocean Model (OCCAM), Sains
      Malays., 41(6), 701–714, 2012.

Alberty, M., Sprintall, J., MacKinnon, J., Germineaud, C., Cravatte, S., and Ganachaud, A.: Moored Observations of Transport in the Solomon
      Sea, J. Geophys. Res. Oceans, 124(11), 8166–8192, 2019.

Aschariyaphotha, N. and Wongwises, S.: Simulations of Seasonal Current Circulations and Its Variabilities Forced by Runoff from Freshwater
555   in the Gulf of Thailand, Arab. J. Sci. Eng., 37(5), 1389–1404, 2012.

Aschariyaphotha, N., Wongwises, P., Wongwises, S., Humphries, U. W., and You, X.: Simulation of Seasonal Circulations and Thermohaline
      Variabilities in the Gulf of Thailand, Adv. Atmos. Sci., 25(3), 489–506, 2008.

Black, E., Slingo, J., and Sperber, K. R.: An Observational Study of the Relationship between Excessively Strong Short Rains in Coastal East
      Africa and Indian Ocean SST, Mon. Wea. Rev., 131, 74 – 94, https://doi.org/10.1175/1520-0493(2003)131<0074:AOSOTR>2.0.CO;2,
560   2003.

Bonjean, F. and Lagerloef, G. S. E.: Diagnostic Model and Analysis of the Surface Currents in the Tropical Pacific Ocean, J. Phys. Oceanogr.,
      32, 2938–2954, 2002.

Buranapratheprat, A., Yanagi, T., and Sawangwong, P.: Seasonal Variations in circulation and Salinity Distributions in the Upper Gulf of
      Thailand, La mer, 40, 147–155, 2002.

565   Buranapratheprat, A., Yanagi, T., Sojisuporn, P., and Booncherm, C.: Influence of local wind field on seasonal circulations in the upper Gulf
      of Thailand, Coast. Mar. Sci., 30(1), 19–26, 2006.

Buranapratheprat, A., Yanagi, T., and Matsumura, S.: Seasonal variation in water column conditions in the upper Gulf of Thailand, Cont.
      Shelf Res., 28, 1509–2522, 2008.

Buranapratheprat, A., Niemann, K. O., Matsumura, S., and Yanagi, T.: MERIS imageries to investigate surface chlorophyll in the upper Gulf
570   of Thailand, Coast. Mar. Sci., 33, 22–28, 2009.

Caruso, M. J., Gawarkiewicz, G. G., and Beardsley, R. C.: Interannual variability of the Kuroshio intrusion in the South China Sea, J.
      Oceanogr., 62, 559–575, https://doi.org/10.1007/s10872-006-0076-0, 2006.

Centurioni, L. R., Niiler, P. N., and Lee, D.-K.: Near-surface circulation in the South China Sea during the winter monsoon, Geophys. Res.
      Lett., 36, https://doi.org/https://doi.org/10.1029/2008GL037076, 2009.

575   Chao, S.-Y., Shaw, P.-T., and Wu, S. Y.: El Niño modulation of the South China Sea circulation, Prog. Oceanogr., 38, 51–93,
      https://doi.org/https://doi.org/10.1016/S0079-6611(96)00010-9, 1996.

Cui, X., Fang, G., and Wu, D.: Tidal resonance in the Gulf of Thailand, Ocean Sci., 15(2), 321–331, 2019.

Delman, A. S., McClean, J. L., Sprintall, J., Talley, L. D., and Bryan, F. O.: Process-Specific Contributions to Anomalous Java Mixed Layer
      Cooling During Positive IOD Events, J. Geophys. Res. Oceans, 123, 4153–4176, https://doi.org/https://doi.org/10.1029/2017JC013749,
580   2018.

Ducet, N., Traon, P. Y. L., and Reverdin, G.: Global high-resolution mapping of ocean circulation from TOPEX/Poseidon and ERS-1 and -2,
      J. Geophys. Res., 105, 19 477–19 498, 2000.

Gan, J., Li, H., Curchitser, E. N., and Haidvogel, D. B.: Modeling South China Sea circulation: Response to seasonal forcing regimes, J.
      Geophys. Res. Oceans, 111, https://doi.org/https://doi.org/10.1029/2005JC003298, 2006.

585 Giddings, S. N. and MacCready, P.: Reverse Estuarine Circulation Due to Local and Remote Wind Forcing, Enhanced by the Presence of Along-Coast Estuaries, J. Geophys. Res. Oceans, 122, 10 184–10 205, https://doi.org/https://doi.org/10.1002/2016JC012479, 2017.

Higuchi, M., Anongponyoshun, M., Phaksopa, J., and Onishi, H.: Influence of monsoon-forced Ekman transport on sea surface height in the Gulf of Thailand, Agr. Nat. Resour., 54, 205–210, https://doi.org/10.34044/j.anres.2020.54.2.12, 2020.

Holgate, S. J., Matthews, A., Woodworth, P. L., Rickards, L. J., Tamisiea, M. E., Bradshaw, E., Foden, P. R., Gordon, K. M., Jevrejeva,
590 S., and Pugh, J.: New Data Systems and Products at the Permanent Service for Mean Sea Level, J. Coastal Res., 29(3), 493–504, https://doi.org/10.2112/JCOASTRES-D-12-00175.1, 2013.

Hu, J., Kawamura, H., Hong, H., and Qi, Y.: A Review on the Currents in the South China Sea: Seasonal Circulation, South China Sea Warm Current and Kuroshio Intrusion, J. Oceanogr., 56, 607–624, https://doi.org/10.1023/A:1011117531252, 2000.

Jilan, S.: Overview of the South China Sea circulation and its influence on the coastal physical oceanography outside the Pearl River Estuary,
595 Cont. Shelf Res., 24, 1745–1760, https://doi.org/https://doi.org/10.1016/j.csr.2004.06.005, pearl River Estuary Study, 2004.

Klinck, J. M.: EOF Analysis of Central Drake Passage Currents from DRAKE 79, J. Phys. Oceanogr., 15, 288 – 298, https://doi.org/10.1175/1520-0485(1985)015<0288:EAOCDP>2.0.CO;2, 1985.

Kubryakov, A. A. and Stanichny, S. V.: Estimating the quality of the retrieval of the surface geostrophic circulation of the Black Sea by satellite altimetry data based on validation with drifting buoy measurements, Izv. Atmos. Ocean. Phys., 490, 930–938, 2013.

600 Kundu, P. K.: Ekman Veering Observed near the Ocean Bottom, J. Phys. Oceanogr., 6, 238 – 242, https://doi.org/10.1175/1520-0485(1976)006<0238:EVONTO>2.0.CO;2, 1976.

Kundu, P. K. and Allen, J. S.: Some Three-Dimensional Characteristics of Low-Frequency Current Fluctuations near the Oregon Coast, J. Phys. Oceanogr., 6, 181 – 199, https://doi.org/10.1175/1520-0485(1976)006<0181:STDCOL>2.0.CO;2, 1976.

Li, J., Zhang, R., Ling, Z., Bo, W., and Liu, Y.: Effects of Cardamom Mountains on the formation of the winter warm pool in the Gulf of
605 Thailand, Cont. Shelf Res., 91, 211–219, 2014.

Liu, Q., Kaneko, A., and Jilan, S.: Recent progress in studies of the South China Sea circulation, J. Oceanogr., 64, 753–762, 2008.

Liu, Q., Feng, M., and Wang, D.: ENSO-induced interannual variability in the southeastern South China Sea, J. Oceanogr., 67, 127–133, https://doi.org/10.1007/s10872-011-0002-y, 2011.

MacCready, P., Pawlak, G., Edwards, K., and McCabe, R.: Form drag on ocean flows, in: Proceedings of the 13th "Aha Huliko"a Hawaiian
610 Winter Workshop: Near-Boundary Processes and their Parameterization, pp. 119–130, University of Hawaii at Monoa, Honolulu, HI, 2003.

Meyers, G.: Variation of Indonesian throughflow and the El Niño-Southern Oscillation, J. Geophys. Res. Oceans, 101, 12 255–12 263, https://doi.org/https://doi.org/10.1029/95JC03729, 1996.

Nan, F., Xue, H., and Yu, F.: Kuroshio intrusion into the South China Sea: A review, Prog. Oceanogr., 137, 314–333,
615 https://doi.org/https://doi.org/10.1016/j.pocean.2014.05.012, 2015.

North, G. R., Bell, T. L., Cahalan, R. F., and Moeng, F. J.: Sampling Errors in the Estimation of Empirical Orthogonal Functions, Mon. Wea. Rev., 110, 699 – 706, https://doi.org/10.1175/1520-0493(1982)110<0699:SEITEO>2.0.CO;2, 1982.

Poulain, P.-M., Menna, M., and Mauri, E.: Surface Geostrophic Circulation of the Mediterranean Sea Derived from Drifter and Satellite Altimeter Data, J. Phys. Oceanogr., 42, 973 – 990, https://doi.org/10.1175/JPO-D-11-0159.1, 2012.

620 PSMSL: "Tide Gauge Data", http://www.psmsl.org/data/obtaining/, 2019.

Saji, N. H., Goswami, B. N., Vinayachandran, P. N., and Yamagata, T.: A dipole in the tropical Indian Ocean, Nature, 401, 360–363, 1999.

Saramul, S.: Seasonal Monsoon Variations in Surface Currents in the Gulf of Thailand Revealed by High Frequency Radar, Eng. J., 21(4), 25–37, 2017.

Saramul, S. and Ezer, T.: On the dynamics of low latitude, wide and shallow coastal system: numerical simulations of the Upper Gulf of Thailand, Ocean Dyn., 64, 557–571, 2014.

Sojisuporn, P., Morimoto, A., and Yanagi, T.: Seasonal variation of sea surface current in the Gulf of Thailand, Coast. Mar. Sci., 34(1), 91–102, 2010.

Sprent, P. and Smeeton, N. C.: Applied Nonparametric Statistical Methods, Chapman and Hall/CRC, 2007.

Sprintall, J., Gordon, A. L., Murtugudde, R., and Susanto, R. D.: A semiannual Indian Ocean forced Kelvin wave observed in the Indonesian seas in May 1997, J. Geophys. Res. Oceans, 105, 17 217–17 230, https://doi.org/https://doi.org/10.1029/2000JC900065, 2000.

Sriwoon, R., Pholpunthin, P., Kishino, M., and Furuya, K.: Population dynamics of green Noctiluca scintillans (Dinophyceae) associated with the monsoon cycle in the upper Gulf of Thailand, J. Phycol., 44, 605 – 615, https://doi.org/10.1111/j.1529-8817.2008.00516.x, 2008.

Suvapepun, S.: Long term ecological changes in the Gulf of Thailand, Mar. Pollut. Bull., 23, 213–217, https://doi.org/https://doi.org/10.1016/0025-326X(91)90677-K, environmental Management and Appropriate Use of Enclosed Coastal Seas, 1991.

Trenberth, K. E.: The Definition of El Niño, Bull. Am. Meteorol. Soc., 78, 2771 – 2778, https://doi.org/10.1175/1520-0477(1997)078<2771:TDOENO>2.0.CO;2, 1997.

Trisirisatayawong, I., Naeije, M., Simons, W., and Fenoglio-Marc, L.: Sea level change in the Gulf of Thailand from GPS-corrected tide gauge data and multi-satellite altimetry, Global Planet. Change, 76, 137–151, 2011.

Wang, B.: Kelvin waves, Encyclopedia of atmospheric sciences, 1062, 2002.

Wang, D., Wang, W., Shi, P., Guo, P., and Gan, Z.: Establishment and adjustment of monsoon-driven circulation in the South China Sea, Sci. China Ser. D, 46, 173–181, https://doi.org/10.1360/03yd9016, 2003.

Wang, Y., Fang, G., Wei, Z., Qiao, F., and Chen, H.: Interannual variation of the South China Sea circulation and its relation to El Niño, as seen from a variable grid global ocean model, J. Geophys. Res. Oceans, 111, https://doi.org/https://doi.org/10.1029/2005JC003269, 2006.

Weare, B. C., Navato, A. R., and Newell, R. E.: Empirical Orthogonal Analysis of Pacific Sea Surface Temperatures, J. Phys. Oceanogr., 6, 671 – 678, https://doi.org/10.1175/1520-0485(1976)006<0671:EOAOPS>2.0.CO;2, 1976.

Wentz, F. J., Scott, J., Hoffman, R., Leidner, M., Atlas, R., and Ardizzone, J.: Remote Sensing Systems Cross-Calibrated Multi-Platform (CCMP) 6-hourly ocean vector wind analysis product on 0.25 deg grid, Version 2.0, 2012-2017. Remote Sensing Systems, Santa Rosa, CA, www.remss.com/measurements/ccmp, 2015.

Wyrtki, K.: Scientific Results of marine investigations of the South China Sea and the Gulf of Thailand 1959–1961, Tech. Rep. 164-169, University of California at San Diego, 1961.

Yanagi, T. and Takao, T.: Clockwise Phase Propagation of Semi-Diurnal Tides in the Gulf of Thailand, J. Oceanogr., 54, 143–150, 1998.

Yanagi, T., Sachoemar, S. I., Takao, T., and Fujiwara, S.: Seasonal Variation of Stratification in the Gulf of Thailand, J. Oceanogr., 57, 461–470, 2001.

Yin, L., Qiao, F., and Zheng, Q.: Coastal-Trapped Waves in the East China Sea Observed by a Mooring Array in Winter 2006, J. Phys. Oceanogr., 44, 576 – 590, https://doi.org/10.1175/JPO-D-13-07.1, 2014.

Yu, Y., Emery, W. J., and Leben, R. R.: Satellite altimeter derived geostrophic currents in the western tropical Pacific during 1992–1993 and their validation with drifting buoy trajectories, J. Geophys. Res. Oceans, 100, 25 069–25 085, https://doi.org/https://doi.org/10.1029/95JC02146, 1995.

660 Zhou, J., Li, P., and Yu, H.: Characteristics and mechanisms of sea surface height in the South China Sea, Global Planet. Change, 88-89, 20–31, 2012.

–flatten
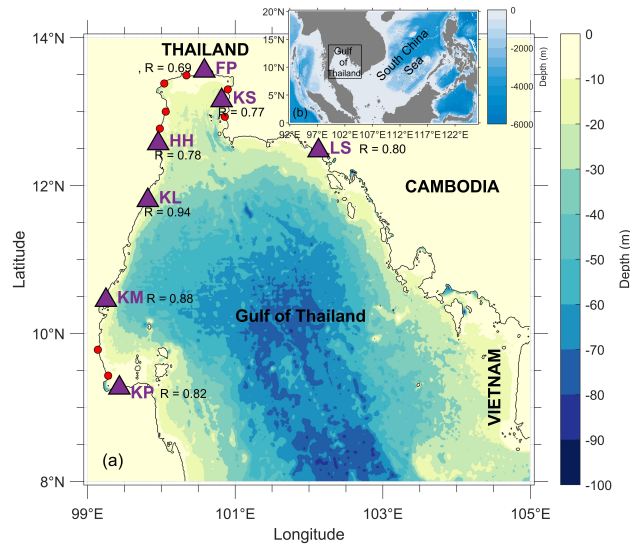
Figure 1. Map of the Gulf of Thailand with the locations of tide gauges (purple triangle) : FP denotes Fort Phrachula Chomklao station, KL denotes Ko Lak station, and KM denotes Ko Mattaphon station high-frequency coastal radar (red circle) (a) and the nearby regions (b). Correlation (R) between sea level measured by the satellite and tide gauges at KP (Ko Prap), KM (Ko Mattaphon), KL (Ko Lak), HH (Huahin), FP (Fort Phrachula Chomklao), KS (Ko Sichang), and LS (Laem Sing) are shown. Color contour represents bathymetry and black contour represents the zero-depth level.
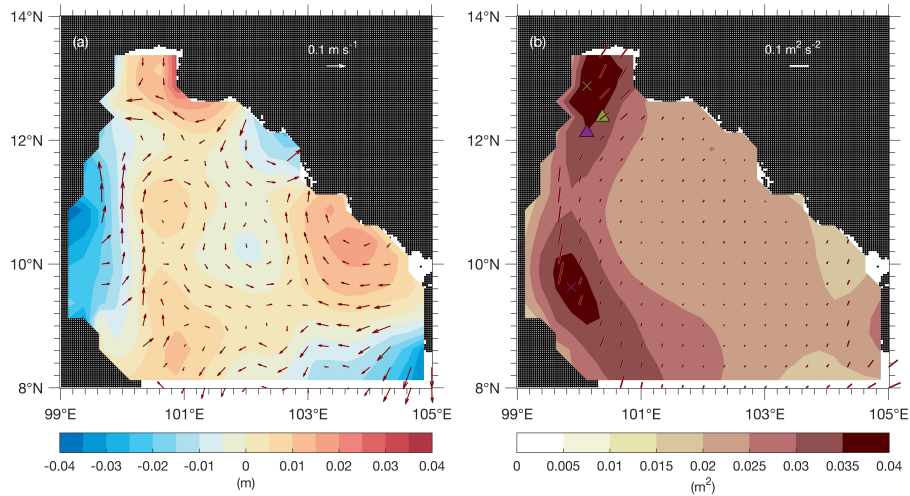
Figure 2. The 2014-2019 mean OSCAR current (shown in maroon quivers)and the 2014-2019 mean ADT (shown in color contour)over the Gulf of Thailand (a) and the OSCAR current variance (shown in maroon)lines where the zonal (meridional) component of the maroon line lines indicates variance of the zonal OSCAR current and the (meridionalcomponent indicates variance of the meridional) OSCAR current and with ADT variance (shown in color contour ;(b). Crosses in (b) mark locations with high ADT variance in the uGoT (green) and at the western central GoT western boundary (purple) and the triangles with respective colors mark the locations of wind stress curls that correlate the best with the ADT shown in Figure 7.
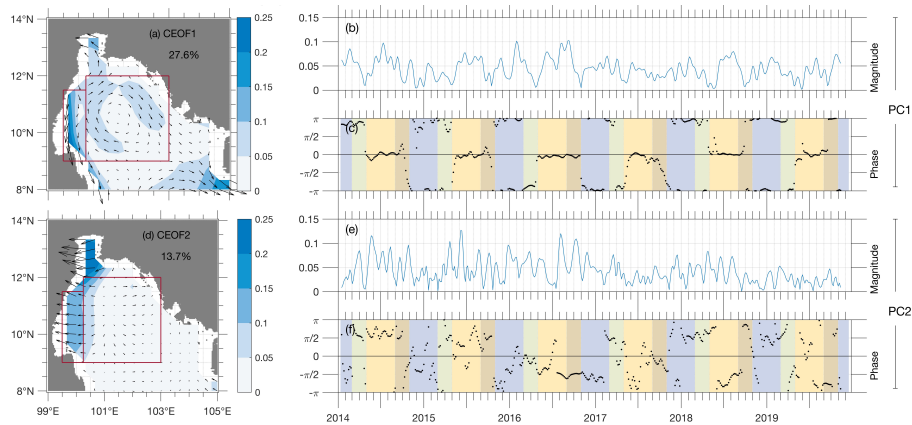
Figure 3. The first (a) and second (d) dominant complex empirical orthogonal function (CEOF) modes of the OSCAR current with the corresponding magnitudes (b), (e) and phases (c), (f) of the principal components (PC). Percentage of the current variance explained by each mode is shown on the upper right corner of (a) and (d). Maroon boxes in (a) and (d) designate the ~~upper Gulf of Thailand region (the northern-most box), the~~ western boundary region (the western-most box) ~~,~~ and the Gulf of Thailand interior region (the eastern-most box). Background shading in (c) and (f) denotes different seasons: northern monsoon (blue), spring monsoon transition (green), southwest monsoon (yellow), and fall monsoon transition (brown).
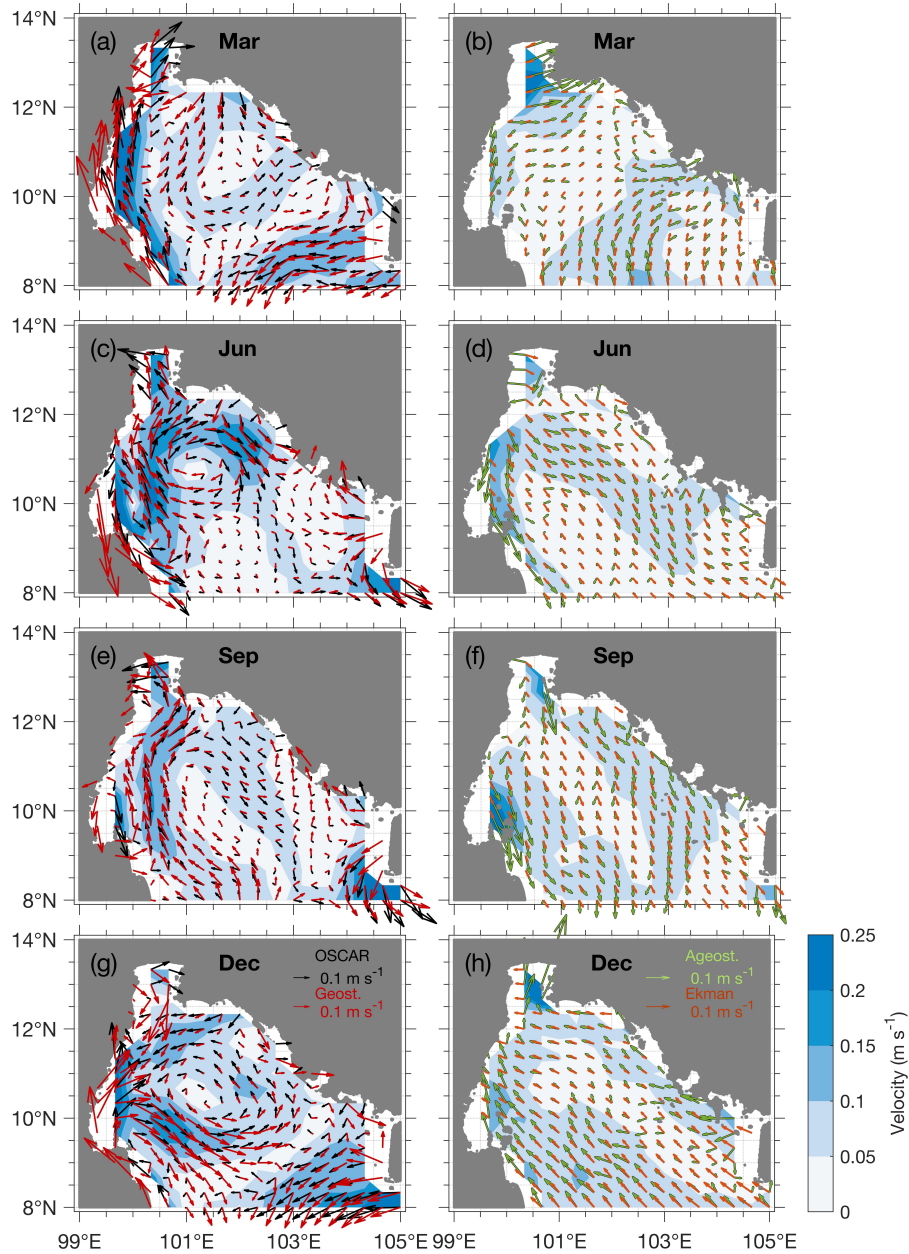
Figure 4. The 2014 - 2019 monthly mean OSCAR current (black; left column), geostrophic current estimated from satellite altimetry (red; left column), ageostrophic flow (green; right column), and wind driven Ekman current (brown; right column) over the Gulf of Thailand in March representing the spring monsoon transition (a) and (b), June representing the southwest monsoon (c) and (d), September representing the fall monsoon transition (e) and (f), and December representing the northeast monsoon (g) and (h). The color contour shown in subplots on the ~~right (~~left (right) column indicates magnitude of the OSCAR (ageostrophic) current ~~and~~ with the color scale presented on the lower right corner. The scale for the current is shown on the upper right corner of (g) and (h).
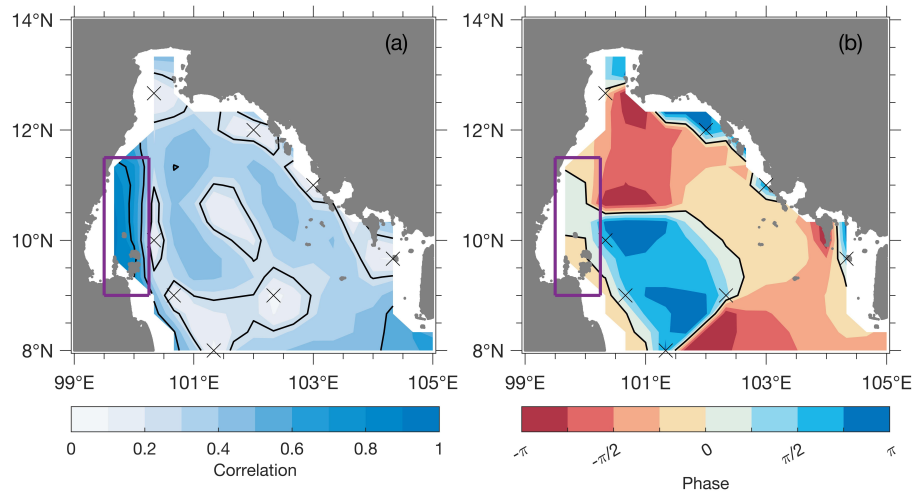
Figure 5. Complex correlation between OSCAR current along the western boundary (purple box) and OSCAR current over the entire Gulf of Thailand (a) and the corresponding phase (b). Black contour in (a) is plotted every 0.25 and that in (b) is plotted at 0 and π. Crosses indicate the regions where the correlation is not significant with the 95% confidence.
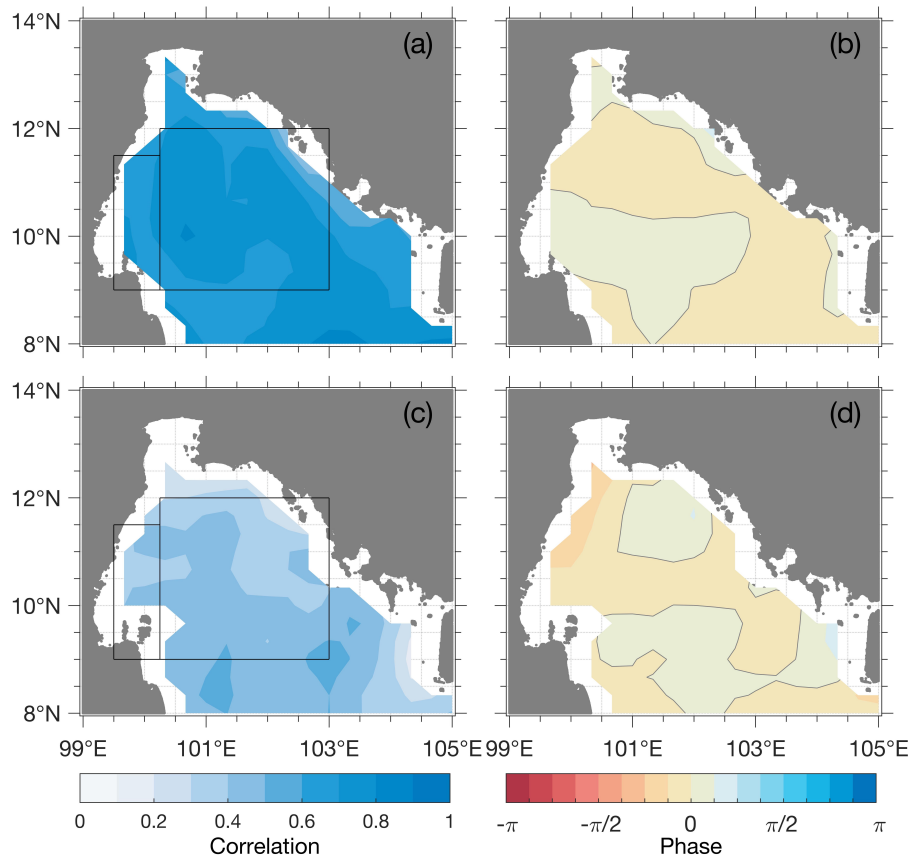
Figure 6. Complex correlation map between the OSCAR current and altimetry-derived geostrophic current (a) and that between ageostrophic current and the Ekman current (c) with the respective phase shown in (b) and (d). Boxes in (a) and (c) designate the western boundary region (the western-most box) and the Gulf of Thailand interior region (the eastern-most box).
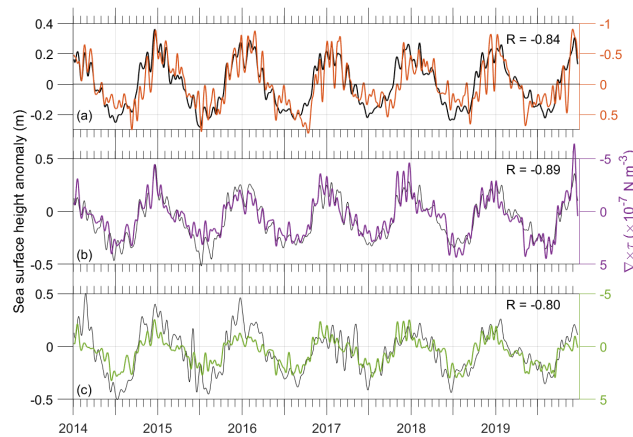
Figure 7. Comparison between sea surface height anomaly (black) and ~~negative~~ wind stress curl (colors): both sea surface height anomaly ~~(black)~~ and wind stress curl (orange) averaged over the entire Gulf of Thailand (a), sea surface height anomaly ~~(black)~~ at the Gulf of Thailand western boundary shown as purple cross in Figure 2b and wind stress curl (purple) to the south of the upper Gulf of Thailand shown as purple triangle in Figure 2b (b), and both sea surface height anomaly ~~(black)~~ and wind stress curl (green) to the south of the upper Gulf of Thailand shown as green cross and triangle in Figure 2b (c). Correlation coefficient between each comparison is shown on the upper right corner of each subplot. Note the reversed y-axis for wind stress curl.
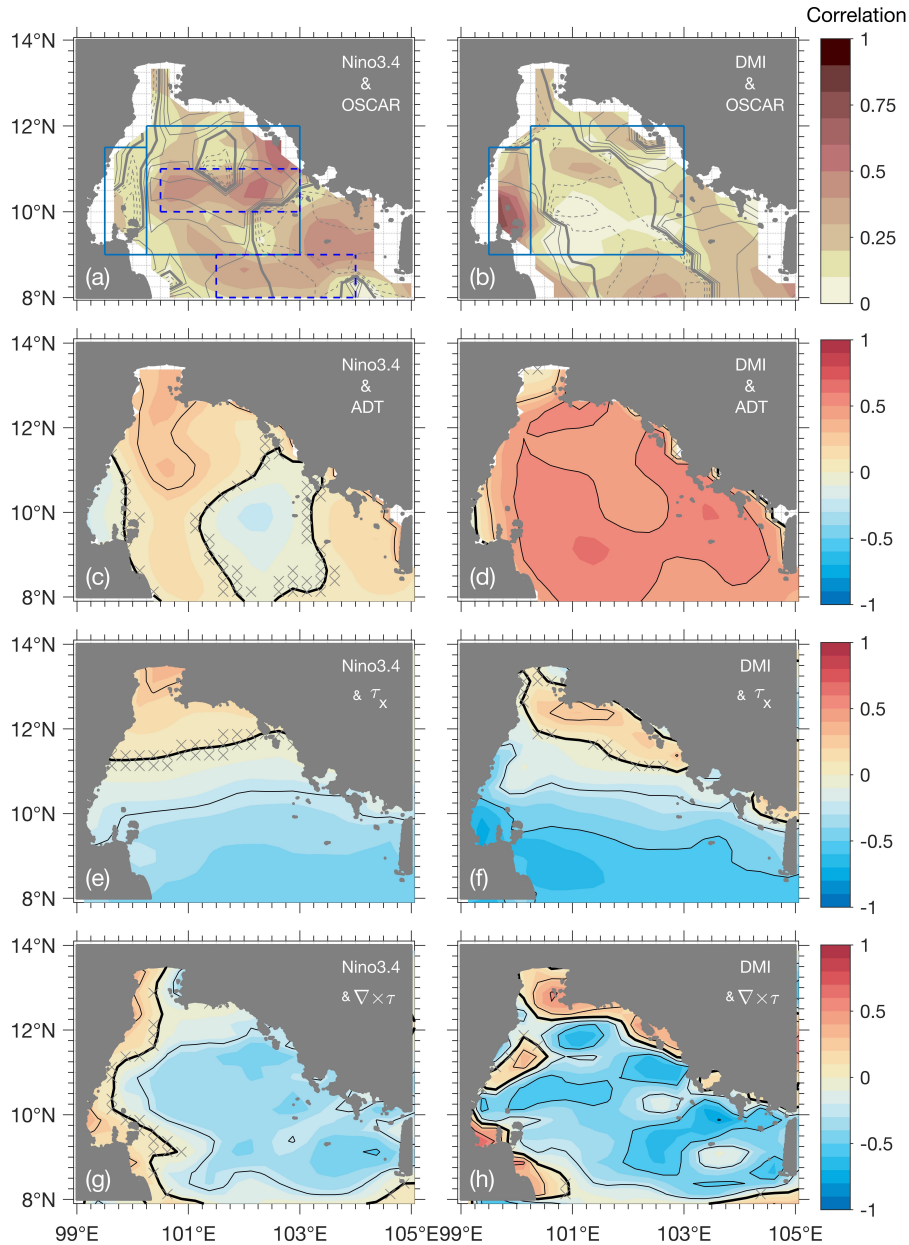
Figure 8. Correlation maps between the Niño 3.4 index and OSCAR current (a), sea surface height (c), zonal wind stress (e), wind stress curl (g), and those between the Dipole Mode Index and OSCAR current (b), sea surface height (d), zonal wind stress (f), wind stress curl (h). ~~Gray contour in~~ Complex correlation was applied to the correlation between OSCAR current and the climate mode indices ((a) and (b)~~shows~~) with gray contour showing the phase associated with the complex correlation map. Solid (dashed) gray line is plotted every $\frac{\pi}{4}$ showing the positive (negative) phase relationship and thick gray line shows the zero contour. The maroon boxes in (a) and (b) designate the ~~upper Gulf of Thailand region (the northernmost box), the~~ western boundary region (the western-most box) ~~,~~ and the Gulf of Thailand interior region (the easternmost box). Dashed maroon boxes in (a) are areas that show high low-frequency variability used in 9c. Thick black contour in (c) – (h) denotes 0 and thin black contour is plotted every 0.25. Crosses in (c) - (h) mark the regions where the correlation is not significant with 95% confidence.
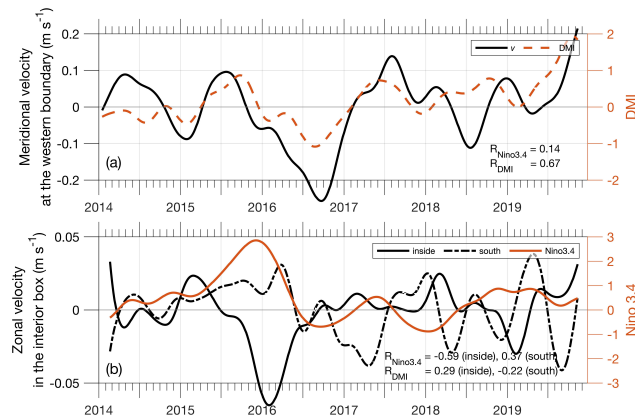
Figure 9. The low-frequency current (black line) representing circulation in the selected regions shown in Figure 8a: mean ~~zonal velocity in the upper Gulf of Thailand (a), mean~~ meridional velocity at the western boundary (~~b~~a) ~~,~~ and mean zonal velocity in the middle of the interior box (solid) and to the south of the box (dashed) (~~c~~b), and the low-frequency climate modes: Niño 3.4 index (solid orange line) and Dipole Mode Index (dashed orange line). Only the climate mode index that shows higher correlation is shown in the corresponding subplot~~(b) and (c)~~. Correlation coefficients between the current and both climate modes are shown on the lower right corner of each subplot; the correlation coefficients between the climate modes and the mean zonal velocity in the middle of interior box are shown as the first values and those with the mean zonal current to the south of the box are shown as the second values.